





Geometry-mediated particle accumulation driven by nonhydrodynamic viscosity effect with flow control implications in porous media

Xukang Lu ¹, Qiangqiang Li,¹ Guang Yang,¹ Yunfan Huang ¹,
Wenhai Lei ² and Moran Wang ^{1,*}

¹*Department of Engineering Mechanics, Tsinghua University, Beijing 100084, China*

²*Department of Engineering Mechanics, KTH Royal Institute of Technology, Stockholm 100 44, Sweden*



(Received 15 January 2025; accepted 22 August 2025; published 25 September 2025)

Understanding and controlling particle transport in porous media is of widespread interest across diverse practical applications. Here, we report geometry-mediated accumulation effect on particle transport under dilute conditions driven by the interplay between particle lagging and viscosity effect, offering an alternative perspective for preferential flow control in porous media. Pore-to-throat velocity variations can trigger strong local accumulation of microgel particles in the absence of clogging effects, which is anomalous given the low Stokes number. Based on volume-averaged equations for two-phase flow, we theoretically elucidate the competition between the drag force representing particle-fluid interactions and an additional resistance force representing interparticle interactions, which governs particle accumulation and becomes significant only with concentration-sensitive viscosity. Differing from shear-induced migration driven by multibody hydrodynamic or collision interactions at higher concentrations, such accumulation occurs only in the presence of geometry variations, highlighting its promising impact on suspension flow in porous media. A new dimensionless number is proposed and validated by numerical simulations in typical pore-throat geometries to generally describe the triggering criterion and accumulation intensity. Investigations in heterogeneous porous media reveal varying accumulation patterns under various injection conditions, which are predictable applying theoretical descriptions. Unexpected preferential flow control performances arise from lateral flow reallocation, controlled by the formation and distribution of localized intense accumulation zones. Our findings provide insights into particle transport mechanisms and flow control strategies in microchannels and porous media.

DOI: [10.1103/834p-q9hf](https://doi.org/10.1103/834p-q9hf)

I. INTRODUCTION

Particle transport in porous media is ubiquitous in numerous natural and industrial scenarios, such as soil remediation [1,2], wastewater treatment [3,4], enhanced hydrocarbon recovery [5,6], and microorganism migration [7,8]. Extensive efforts have been made to understand the retention and clogging mechanisms of particles [9–12], which significantly distinguish particle migration from solute transport in porous media. Particle clogging has been widely utilized to suppress preferential flow since retained particles can partially block the mainstream pathways and divert fluid into low-permeability regions [13–15]. However, severe clogging with uncontrollable particle retention and permeability reduction can hinder sustainable fluid flow [16].

Particle lagging and accumulation in the absence of clogging are commonly associated with inertial effects [17–19]. The inertia of fluid is characterized by the fluid Reynolds number

*Contact author: mrwang@tsinghua.edu.cn

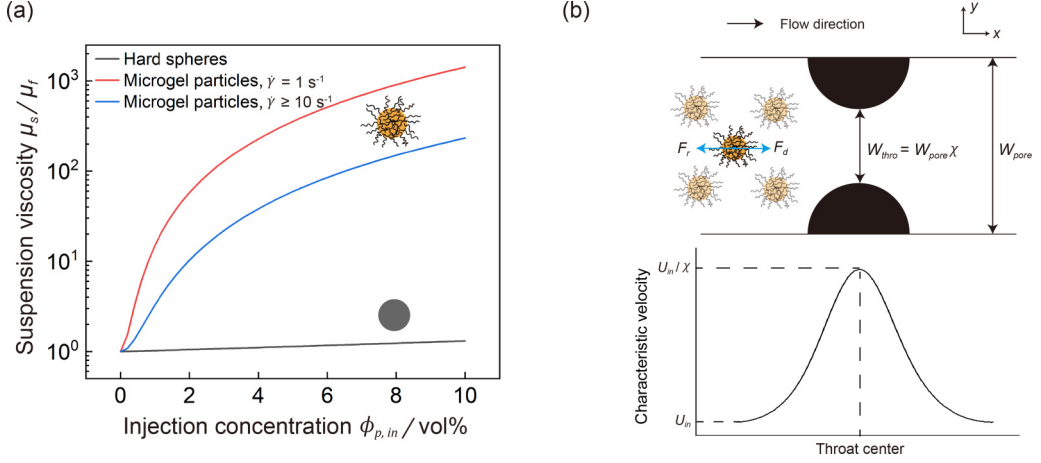


FIG. 1. Origin of the geometry-mediated accumulation effect. (a) Comparison of concentration-dependent viscosities of typical particle systems in dilute conditions. The strong interparticle interactions induced by the polymeric network structure are responsible for the concentration sensitivity of microgel particle suspensions. The rheological properties of hard-sphere and microgel particle suspensions are from Krieger and Dougherty’s model and Eq. (1), respectively. (b) Illustration of the competition between fluid drag and the resistance force representing interparticle interactions in a typical pore-throat geometry with velocity variations.

$Re_f = \rho_f UL/\mu_f$, while the inertia of particles is described by the particle Stokes number $Stk = t_0 U_f/L$, where ρ_f is the fluid density, U is the characteristic velocity, L is the characteristic length of the system, μ_f is the dynamic viscosity of the fluid, and t_0 is the relaxation time of the particle. For Stokes flow, t_0 is given by $\rho_p d_p^2/(18\mu_f)$, where ρ_p is the particle density and d_p is the particle diameter. Given that $Stk = \frac{1}{18}(\frac{d_p}{L})^2 Re_f$ under density-matched condition, inertia effects on particle transport in porous media should be negligible as $Re_f \ll 1$ and thus $Stk \ll 1$ when $d_p < L$.

The Stokes number primarily accounts for the role of fluid drag in redirecting particle trajectories. The impacts of interparticle interactions [20,21], which introduce additional resistance compared to a single particle in open space and manifest as concentration-dependent viscosity, have not been included in the definition of Stokes number. Although interphase drag can be sufficiently large to overcome particle inertia at a low Stokes number, resistance from interparticle interactions can prevent particles from perfect advection, which may naturally induce particle lagging and concentration redistribution.

Shear-induced migration is a widely studied phenomenon of concentration redistribution that can occur under Stokes flow conditions. For pressure-driven flow in a straight channel, particles spontaneously migrate towards the region with a lower shear rate, leading to particle accumulation near the channel center [22,23]. Previous studies have shown that this behavior is driven by the divergence of particle phase stress, which depends on local shear conditions and is dominated by multibody hydrodynamic or collision interactions among particles [24–26]. As a result, shear-induced migration is typically observed at moderate to high particle concentrations [27], where such interactions become significant. The focus of this study, however, is to explore whether and under what conditions particle accumulation can be dramatic at dilute concentrations.

The apparent rheological property of suspensions offers a macroscopic view of microscopic interparticle interactions [20]. Figure 1(a) presents concentration dependences of suspension viscosity in dilute conditions ($< 10 \text{ vol\%}$). For ideal hard-sphere systems, a weak viscosity effect is expected, indicating insignificant interparticle interactions as particles are far away from each other. Krieger

and Dougherty's model [28] is adopted here, which gives

$$\frac{\mu_s}{\mu_f} = (1 - \phi_p/\phi_{\text{lim}})^{-2.5\phi_{\text{lim}}}, \quad (1)$$

where μ_s is the suspension viscosity, ϕ_p is the particle volume fraction, and $\phi_{\text{lim}} \approx 0.64$. There are also other empirical models yielding better performances at high volume fractions [27], which hardly influence discussions in this study since we focus on dilute conditions (See the Supplemental Material [29] for a more detailed comparison).

In certain complex particle systems such as blood [30] and gel particle dispersions [15], the suspension viscosity can be highly sensitive to particle concentration even in dilute conditions. Such viscosity effects reflect nonhydrodynamic interparticle interactions, and differ from the multibody hydrodynamic or collision interactions mentioned above. Specifically, microgel particles composed of a cross-linked polymeric network can cause a significant viscosity increase, as the hydrophilic surface chains will extend in water and interact with each other [31]. The concentration-dependent non-Newtonian rheology induced by nonhydrodynamic effects has been included in a fitting expression based on systematic experimental characterizations at varying shear rates and microgel concentrations [32,33],

$$\frac{\mu_s}{\mu_f} = \begin{cases} (142\phi_p^2 - 0.2\phi_p)\dot{\gamma}^{-0.786} \times 10^3 + 1, & \dot{\gamma} < 10 \text{ s}^{-1} \\ 163(142\phi_p^2 - 0.2\phi_p) + 1, & \dot{\gamma} \geq 10 \text{ s}^{-1}, \end{cases} \quad (2)$$

where $\dot{\gamma}$ is the shear rate.

For microgel particle suspensions with such concentration-sensitive viscosity, the resistance force F_r representing interparticle interactions can be strong enough to compete with the drag force F_d representing fluid-particle interactions, impeding particle mobilization. For steady flow in a straight channel, this force competition creates a steady velocity difference between the particle and fluid phases. However, as demonstrated in Fig. 1(b), geometric variations from pores to throats during flow in porous media may naturally induce flow condition variations, which can break the local force balance and lead to redistribution of particle concentration.

It is noteworthy that some previous pore-scale microfluidic experiments and core-scale flooding experiments have reported dramatic particle accumulation in porous media when applying dilute suspensions of microgel particles (injection concentration ≤ 3 vol %) [33–35], despite the small particle-to-throat size ratio and negligible adsorption effect. This phenomenon was considered anomalous and cannot be simply explained by either retention behaviors or rheology changes. Simulations based on advection-diffusion equations, which treat the suspension as a polymer solution with non-Newtonian rheology, have failed to capture the accumulation and corresponding multiphase displacement patterns [33]. The accumulation mechanisms and implications for flow control in porous media remain poorly understood. Hence, the coupling effect of particle lagging behaviors and suspension property variations should be further analyzed.

The continuum-mechanical descriptions based on the volume-averaging approach for two-phase flow provide a powerful tool for investigating suspension flow [36], which have been applied in various models such as the two-fluid model (TFM) developed for simulating fluidized beds [20,37], and the suspension balance model proposed for capturing shear-induced migration [24]. Although the continuum approach is more commonly applied to the flow of dense suspensions, it is also well suited for capturing accumulation effects in dilute conditions with strong nonhydrodynamic viscosity effects, as the significant interparticle interactions can be effectively characterized by the particle phase stress. Despite the promising potential for studying collective transport of particles, the force balance determining particle accumulation in porous media, particularly the role of the resistance term, has not been clarified.

In this work, inspired by anomalous accumulation phenomena reported in previous experiments [33–35], we discover and elucidate geometry-mediated accumulation driven by nonhydrodynamic viscosity effects combining theoretical analysis and numerical simulations, which significantly

reshapes particle transport and fluid flow in porous media. Concentration-sensitive viscosity and velocity variations induced by geometry changes in porous media are identified as two prerequisites for the occurrence of accumulation. A dimensionless number is derived from volume-averaged governing equations to quantify the triggering condition and intensity of particle accumulation. Simulations in typical pore-throat geometries confirm the validity of our theoretical model and generality of the accumulation mechanism. Simulations in dual-permeability porous structures reveal transitions in accumulation patterns and preferential flow control performances under various injection conditions. The relationships between microscopic force balances, pore-scale accumulation states, and macroscopic flow consequences are comprehensively analyzed.

II. GOVERNING EQUATIONS FOR THE TWO-PHASE MODEL

We quantitatively characterize particle transport and accumulation behaviors using volume-averaged equations of particulate two-phase flow. The suspended particles and fluid are both treated as continuum phases with a spatial distribution of volume fractions. The governing equations for the particle, fluid, and suspension (mixture) phases have been rigorously derived based on volume-averaging approaches in previous studies [24,26,38]. As the suspension phase is composed of the particle and fluid phases, only two of the three momentum balances are independent [38].

The governing equations for the three phases are given as

$$\frac{\partial(\phi_p \rho_p)}{\partial t} + \nabla \cdot (\phi_p \rho_p \mathbf{u}_p) = 0, \quad (3a)$$

$$\frac{\partial(\phi_p \rho_p \mathbf{u}_p)}{\partial t} + \nabla \cdot (\phi_p \rho_p \mathbf{u}_p \mathbf{u}_p) = -\phi_p \nabla P + \nabla \cdot (\phi_p \mathbf{\Gamma}_p) + \beta(\mathbf{u}_f - \mathbf{u}_p) + \mathbf{F}_{\text{ext},p}, \quad (3b)$$

$$\frac{\partial(\phi_f \rho_f)}{\partial t} + \nabla \cdot (\phi_f \rho_f \mathbf{u}_f) = 0, \quad (4a)$$

$$\frac{\partial(\phi_f \rho_f \mathbf{u}_f)}{\partial t} + \nabla \cdot (\phi_f \rho_f \mathbf{u}_f \mathbf{u}_f) = -\phi_f \nabla P + \nabla \cdot (\phi_f \mathbf{\Gamma}_f) - \beta(\mathbf{u}_f - \mathbf{u}_p) + \mathbf{F}_{\text{ext},f}, \quad (4b)$$

$$\frac{\partial \rho_s}{\partial t} + \nabla \cdot (\rho_s \mathbf{u}_s) = 0, \quad (5a)$$

$$\frac{\partial(\rho_s \mathbf{u}_s)}{\partial t} + \nabla \cdot (\rho_s \mathbf{u}_s \mathbf{u}_s) = -\nabla P + \nabla \cdot \mathbf{\Gamma}_s + \mathbf{F}_{\text{ext}}, \quad (5b)$$

where the subscripts p , f , and s indicate the fluid, particle, and suspension phases, and ϕ , ρ , P , β , \mathbf{u} , \mathbf{F}_{ext} are the volume fraction, phase density, pressure, drag force coefficient, velocity, and external forces, respectively. $\mathbf{\Gamma}_i = \mu_i [\nabla \mathbf{u}_i + (\nabla \mathbf{u}_i)^T]$ is the viscous stress tensor, where ∇ denotes the gradient operator with respect to the spatial vector \mathbf{x} . Note that $\phi_f + \phi_p = 1$ and $\rho_s \mathbf{u}_s = \rho_f \phi_f \mathbf{u}_f + \rho_p \phi_p \mathbf{u}_p$.

Under the continuum-mechanical framework, fluid-particle interactions are reflected by the drag force term, $\mathbf{F}_d = \beta(\mathbf{u}_f - \mathbf{u}_p)$. Note that the particle phase viscosity μ_p in the viscous term of Eq. (3b), $\mathbf{F}_r = \nabla \cdot \{\phi_p \mu_p [\nabla \mathbf{u}_p + (\nabla \mathbf{u}_p)^T]\}$, does not mean a real viscosity like that of the fluid phase. Instead, it serves as a characterization of the internal stress transfer and momentum diffusion effects within the particle phase. In fluidized bed modeling, it is directly linked to the random fluctuations and collisions of particles [39,40]. For dilute suspension transport discussed in this work, the particle phase viscosity is usually very small for hard spheres due to negligible roles of the multibody hydrodynamic or collision interactions among particles [26,27]. However, it can increase significantly for microgel particles, which essentially reflects nonhydrodynamic interparticle interactions attributed to the polymeric nature [31,33], and can be associated with the apparent rheological property of the suspension.

Considering steady flow without additional external forces (such as gravity) and under density-matched condition ($\rho_f = \rho_p = \rho_s = \rho$), all time derivative terms and external force terms can be

omitted. By introducing dimensionless physical quantities $\mathbf{x}^* = \mathbf{x}/L$, $\mathbf{u}_i^* = \mathbf{u}_i/U$, $P^* = P/P_0$, and collecting the coefficients, the governing equations can be expressed in the following nondimensional forms:

$$\nabla^* \cdot (\phi_p \mathbf{u}_p^*) = 0, \quad (6a)$$

$$\frac{\rho UL}{\mu_f} \nabla^* \cdot (\phi_p \mathbf{u}_p^* \mathbf{u}_p^*) = -\frac{P_0 L}{U \mu_f} \phi_p \nabla^* P^* + \nabla^* \cdot \left(\phi_p \frac{\mu_p}{\mu_f} \left(\nabla^* \mathbf{u}_p^* + (\nabla^* \mathbf{u}_p^*)^T \right) \right) + \frac{\beta L^2}{\mu_f} (\mathbf{u}_f^* - \mathbf{u}_p^*), \quad (6b)$$

$$\nabla^* \cdot (\phi_f \mathbf{u}_f^*) = 0, \quad (7a)$$

$$\frac{\rho UL}{\mu_f} \nabla^* \cdot (\phi_f \mathbf{u}_f^* \mathbf{u}_f^*) = -\frac{P_0 L}{U \mu_f} \phi_f \nabla^* P^* + \nabla^* \cdot \left[\phi_f \left(\nabla^* \mathbf{u}_f^* + (\nabla^* \mathbf{u}_f^*)^T \right) \right] - \frac{\beta L^2}{\mu_f} (\mathbf{u}_f^* - \mathbf{u}_p^*), \quad (7b)$$

$$\nabla^* \cdot \mathbf{u}_s^* = 0, \quad (8a)$$

$$\frac{\rho UL}{\mu_f} \nabla^* \cdot (\mathbf{u}_s^* \mathbf{u}_s^*) = -\frac{P_0 L}{U \mu_f} \nabla^* P^* + \nabla^* \cdot \left(\frac{\mu_s}{\mu_f} \nabla^* \mathbf{u}_s^* + (\nabla^* \mathbf{u}_s^*)^T \right). \quad (8b)$$

Note that all terms are normalized by the coefficient of the viscous term of the fluid phase since μ_f is a constant, while ϕ_p , ϕ_f , μ_p , and μ_s can vary with the particle concentration distribution, and are thus included within the spatial derivative terms. The above nondimensional equation sets show several key dimensionless groups: $\text{Re}_f = \rho UL/\mu_f$ is the fluid Reynolds number; $P_0 L/(U \mu_f)$ and $\beta L^2/\mu_f$ characterize the relative magnitude of the applied pressure gradient and the interphase drag to the divergence of the viscous stress of the fluid phase, respectively; and μ_p/μ_f and μ_s/μ_f characterize the ratios of particle and suspension viscosities to the fluid viscosity.

In numerical simulations that fully resolve the suspension flow, it is sufficient to solve equation sets for any two of the three phases. As μ_f and μ_s can be explicitly determined, we choose to solve the governing equations for the fluid phase, Eqs. (7a) and (7b), and the suspension phase, Eqs. (8a) and (8b), respectively. Information regarding the particle phase (ϕ_p and \mathbf{u}_p) is then obtained from local mass ($\phi_f + \phi_p = 1$) and momentum ($\rho_s \mathbf{u}_s = \rho_f \phi_f \mathbf{u}_f + \rho_p \phi_p \mathbf{u}_p$) conservations, which serves as an input for the drag force calculation. Detailed discussions on the modeling strategy and setup are provided in Sec. III.

To identify the essential mechanism driving particle accumulation and to propose feasible criteria for the critical condition, we theoretically analyze the momentum balance of the particle phase Eq. (6b), as detailed in Sec. IV.

For the viscosity models, we only need μ_f and μ_s in numerical simulations, where $\mu_f = 1$ mPa s is fixed, and μ_s is calculated from Eqs. (1) and (2) for hard-sphere and microgel particle suspensions, respectively. In theoretical calculations, we use $\mu_p \approx (\mu_s - \phi_f \mu_f)/\phi_p$ as an estimate of the characteristic particle phase viscosity. For the drag force coefficient, we adopt the classical Wen-Yu model [41] in both numerical simulations and theoretical calculations, which gives $\beta = 3C_d \rho_f \phi_f^{-1.65} \phi_p |\mathbf{u}_f - \mathbf{u}_p|/(4d_p)$, where $C_d = 24(1 + 0.15\text{Re}_d^{0.687})/\text{Re}_d$ and $\text{Re}_d = \rho_f \phi_f d_p |\mathbf{u}_f - \mathbf{u}_p|/\mu_f$. It should be noted that β is independent of velocity ($C_d |\mathbf{u}_f - \mathbf{u}_p|$ is constant) under the low-Reynolds-number condition of interest. See the Supplemental Material [29] for more detailed discussions on constitutive functions and model parameters.

III. NUMERICAL MODELING OF PARTICLE TRANSPORT

The simulations are performed in two dimensions utilizing the TFM based on the volume-averaged equations introduced above. In the conventional TFM, the governing equations for the particle phase, Eqs. (6a) and (6b), and the fluid phase, Eqs. (7a) and (7b), are solved, which has been widely applied in simulations of fluidized beds [20]. An important issue in applying the conventional TFM is to formulate the stress tensor in the viscous resistance term of the particle phase. The

kinetic theory of granular flow has been commonly employed [42,43], which characterizes the microscopic behaviors of particles. However, the model construction is quite complex and still with adjustable parameters. More importantly, such formulation process can be challenging for complex particle systems such as red blood cell and microgel particle suspensions. Meanwhile, the apparent rheological properties of the suspension phase can be conveniently characterized and applied to dilute suspension flow.

A mixture-rheology two-fluid model based on the lattice Boltzmann method has thus been proposed in our previous work [32], which instead solves the fluid phase, Eqs. (7a) and (7b) and the suspension phase, Eqs. (8a) and (8b). Therefore, measurable suspension viscosity [Eqs. (1) and (2)] can be directly utilized without introducing additional empirical models, which particularly benefits investigations into non-hard-sphere particle systems with complex rheological properties.

The reliability of our model has been quantitatively verified by a series of theoretical benchmarks and microfluidic experiments [32], especially in capturing particle lagging and accumulation under porous flow conditions. Details of the numerical algorithm, experimental validations, simulation, and case setup are provided in the Supplemental Material [29].

All simulation cases are conducted under extremely small particle-to-throat size ratios ($\leq 1/80$ for pore-throat geometries and $\leq 1/10$ for the dual-permeability porous medium). On the one hand, direct clogging by size exclusion or bridging can be ignored under such geometric restrictions [9]. On the other hand, deposition-induced accumulation is insignificant for the micron-sized particles with particle-wall electrostatic repulsions [44]. Since clogging effects are not incorporated in the two-fluid model, the nonuniform concentration distribution presented in simulation results can only be induced by the accumulation mechanism proposed in this work. Deformation of microgel particles should be negligible considering the small particle-to-channel size ratio, low characteristic speed, and dilute injection concentration.

IV. THEORETICAL ANALYSIS OF GEOMETRY-MEDIATED ACCUMULATION

In this section, we present a scaling analysis to identify the key force competition determining particle accumulation, and provide a mechanistic interpretation of how geometry-mediated accumulation can be triggered by pronounced nonhydrodynamic viscosity effects in dilute suspension flow. Following reduction of the momentum balance, we derive a characteristic accumulation number that can be directly calculated from the input flow, structure, and particle properties, thus serving as a practical theoretical criterion.

We start from the nondimensional momentum equation for the particle phase [Eq. (6b)]. Considering the Stokes flow condition for transport in porous media ($\text{Re}_f \ll 1$), we have

$$-\frac{P_0 L}{U \mu_f} \phi_p \nabla^* P^* + \nabla^* \cdot \left(\phi_p \frac{\mu_p}{\mu_f} \left(\nabla^* \mathbf{u}_p^* + (\nabla^* \mathbf{u}_p^*)^T \right) \right) + \frac{\beta L^2}{\mu_f} (\mathbf{u}_f^* - \mathbf{u}_p^*) = 0. \quad (9)$$

The pressure gradient term on the left-hand side can be determined from the momentum balance of the suspension phase [Eq. (8b)] as

$$\frac{P_0 L}{U \mu_f} \nabla^* P^* = \nabla^* \cdot \left(\frac{\mu_s}{\mu_f} \nabla^* \mathbf{u}_s^* + (\nabla^* \mathbf{u}_s^*)^T \right). \quad (10)$$

Substituting Eq. (10) into Eq. (9) gives

$$-\phi_p \nabla^* \cdot \left(\frac{\mu_s}{\mu_f} \nabla^* \mathbf{u}_s^* + (\nabla^* \mathbf{u}_s^*)^T \right) + \nabla^* \cdot \left(\phi_p \frac{\mu_p}{\mu_f} \left(\nabla^* \mathbf{u}_p^* + (\nabla^* \mathbf{u}_p^*)^T \right) \right) + \frac{\beta L^2}{\mu_f} (\mathbf{u}_f^* - \mathbf{u}_p^*) = 0. \quad (11)$$

For suspensions with pronounced nonhydrodynamic viscosity effect, where the suspension viscosity is sensitive to particle concentration even under dilute conditions, as in the case of microgel particle suspensions [see Fig. 1(a)], we have $\mu_s \gg \mu_f$ while $\phi_p \ll \phi_f$, leading to $\mu_p \gg \mu_s$.

Consequently, the first term on the left-hand side can be ignored. Then we can rewrite Eq. (11) as

$$\nabla^* \cdot \left(\phi_p \frac{\mu_p}{\mu_f} \left(\nabla^* \mathbf{u}_p^* + (\nabla^* \mathbf{u}_p^*)^T \right) \right) + \frac{\beta L^2}{\mu_f} (\mathbf{u}_f^* - \mathbf{u}_p^*) = 0. \quad (12)$$

Therefore, although the overall suspension flow is governed by the balance between the pressure gradient and viscous resistance, the drag force term \mathbf{F}_d and the viscous resistance term \mathbf{F}_r in the particle phase momentum balance dominate the force competition determining particle accumulation, which essentially reflects the competition between particle-fluid interactions and interparticle interactions. We have validated the force balance by statistics from numerical results, which directly illustrate the relative magnitudes of the different terms. Details are provided in the Supplemental Material [29].

The dimensionless parameter $\beta L^2/\mu_f$ does not explicitly account for particle viscosity effects, which are instead included in μ_p/μ_f . To provide a comprehensive dimensionless number that directly characterizes the accumulation effect, we consider the state before accumulation occurs as the triggering condition, where the particle concentration ϕ_p is spatially uniform. For hard-sphere suspensions [Eq. (1)], μ_s and μ_p depend solely on ϕ_p . For microgel particles [Eq. (2)], $\mu_s = \mu_s(\phi_p, \dot{\gamma})$ and we can take U/L as the characteristic shear rate in theoretical calculations. Then we can simplify Eq. (12) into

$$\nabla^{*2} \mathbf{u}_p^* + \frac{\beta L^2}{\phi_p \mu_p} (\mathbf{u}_f^* - \mathbf{u}_p^*) = 0. \quad (13)$$

It is clear that when particle phase viscosity μ_p is small (corresponding to a weak particle effect on suspension rheology), the drag force can easily overcome the viscous resistance with a minimal interphase velocity difference. However, the velocity difference has to increase dramatically to balance the strengthened resistance when viscosity effect becomes pronounced. As discussed in the introduction, the classical shear-induced migration is essentially driven by variations in the intensity of hydrodynamic or collision interactions in response to the local shear gradient, which play minor roles in dilute conditions. Indeed, even if viscosity effect becomes pronounced, the force competition presented above will only produce a large interphase drift velocity for steady flow in a straight channel, without potential accumulation or migration effects. However, during typical pore-to-throat fluid acceleration in porous media, a reduction in the characteristic channel size can break the force balance, leading to an increase in $(\mathbf{u}_f^* - \mathbf{u}_p^*)/\mathbf{u}_p^*$ based on Eq. (13), where the scalar u denotes the velocity in the mainstream direction. From the momentum conservation, $\mathbf{u}_s^* = \phi_p \mathbf{u}_p^* + (1 - \phi_p) \mathbf{u}_f^*$, the equilibrium particle concentration will rise in response to geometric and flow condition variations, triggering local lagging and accumulation. The use of dimensionless variables here indicates that the mechanism is not influenced by the magnitude of velocity. Such accumulation is further enhanced considering the concentration sensitivity of viscosity, as an increase in ϕ_p can dramatically raise μ_p .

Based on the above interpretations, we define the accumulation effect discussed in this work as “geometry mediated” and “driven by nonhydrodynamic viscosity effect.” A dimensionless number is proposed to conveniently predict the occurrence of such accumulation as $A_g = F_r/F_d \sim \phi_p \mu_p / (\beta L^2)$, so that a higher A_g corresponds to stronger accumulation, where the subscript g denotes the role of geometry variations.

For 2D Poiseuille channel flow, the Laplacian of velocity can be analytically given as $12U/L^2$, where $U = \int u(y) dy / L$. We modify the coefficient accordingly for the convenience of comparison between theoretical predictions and simulations. For the typical pore-throat geometry illustrated in Fig. 1(b), characteristic quantities at the throat are applied under fixed pore inlet properties to account for the geometry change. The accumulation number can thus be expressed as a function of flow, structure, and particle property parameters as

$$A_g = \frac{12\phi_p \mu_p}{\beta W_{\text{pore}}^2 \chi^2}, \quad (14)$$

where W_{pore} is the pore diameter and χ is the throat-to-pore ratio. By substituting the Wen-Yu model, we have

$$A_g = \frac{16\mu_p d_p}{C_d \rho_f (1 - \phi_p)^{-1.65} U_{\text{in}} W_{\text{pore}}^2 \chi}, \quad (15)$$

where U_{in} is the average suspension velocity at the pore inlet and we take U_{in}/χ as the characteristic velocity corresponding to the accumulation condition. As mentioned in Sec. II, $\beta \propto C_d U_{\text{in}}$ is nearly independent of velocity under low-Reynolds-number condition, which means A_g is not explicitly dependent on velocity.

Based on Eq. (15), we can conveniently determine the impacts of various factors on geometry-mediated accumulation for any particle system with a given rheological property. In addition to the explicit dependence on the geometric and particle property conditions, the shear-rate dependence of the viscosity of microgel particle suspensions [Eq. (1)] can introduce flow rate effects. A lower characteristic speed results in a lower shear rate, a higher suspension viscosity, and thus a higher A_g , corresponding to strengthened accumulation.

V. NUMERICAL RESULTS AND DISCUSSION

A. Accumulation states in pore-throat geometries

We first show the accumulation patterns in typical pore-throat geometries to examine the reliability of the proposed accumulation mechanism and the accumulation number. A total of 72 numerical tests are conducted with the input parameters varied in the following range: $U_{\text{in}} = 10^{-4}$ – 10^{-2} m/s, $d_p = 3$ – 6 μm , $\phi_{p,\text{in}} = 1.0$ – 3.0 vol %, $\chi = 0.4$ – 0.6 . The pore size is fixed at 1200 μm , and the smallest throat size is much larger than the maximum particle size. Note that $\text{Stk} = \rho_p U_{\text{in}} d_p^2 / (18\mu_f W_{\text{pore}}) \ll 1$ holds under all tested conditions. To highlight the importance of concentration-sensitive viscosity, we compare the accumulation states of hard-sphere and microgel particle suspensions applying their distinctly different rheological properties.

As exemplified in Fig. 2(a), numerical results exhibit trends consistent with theoretical predictions from A_g . Particle accumulation is concentrated at the pore-to-throat entrance, which corresponds to fluid acceleration and particle lagging. All examples are from cases involving microgel particle suspensions, as the concentration field remains uniform for hard-sphere suspensions under the same conditions. As expected from the theoretical analysis, stronger accumulation is observed as the characteristic speed and throat-to-pore ratio decrease, while particle size and injection concentration increase.

We also confirm the irrelevance of geometry-mediated accumulation to shear-induced migration by comparison in different geometries under the same conditions [Figs. 2(b) and 2(c)]. A uniform concentration distribution is observed for pressure-driven flow in the straight channel, in contrast to the center-concentrated distribution reported in previous studies regarding shear-induced migration [24]. Meanwhile, significant accumulation occurs in the pore-throat geometry with concentration variations along the flow direction.

As summarized in Fig. 2(d), the normalized maximum concentration $\phi_{p,\text{max}}/\phi_{p,\text{in}}$ increases dramatically as A_g increases for microgel particle suspensions, indicating enhanced accumulation at higher A_g . In contrast, $\phi_{p,\text{max}} \approx \phi_{p,\text{in}}$ and $A_g \ll 1$ consistently hold for hard-sphere suspensions, suggesting that geometry-mediated accumulation is hardly triggered with weak viscosity effects. It is confirmed that $A_g > 0.01$ can be applied as the criterion for the triggering condition. We quantify the intensity of accumulation by introducing the normalized standard deviation $\sigma_p/\phi_{p,\text{in}}$, where σ_p is the standard deviation of particle concentration. Figure 2(e) shows that the accumulation intensity of microgel particle suspensions exhibits a scaling dependence on A_g ($\sigma_p/\phi_{p,\text{in}} \sim A_g^{0.7}$, $R^2 = 0.95$). The slight scattering of data points can be attributed to the nonlinear rheological property, irregular pore-throat geometry, and wide range of input parameter sets.

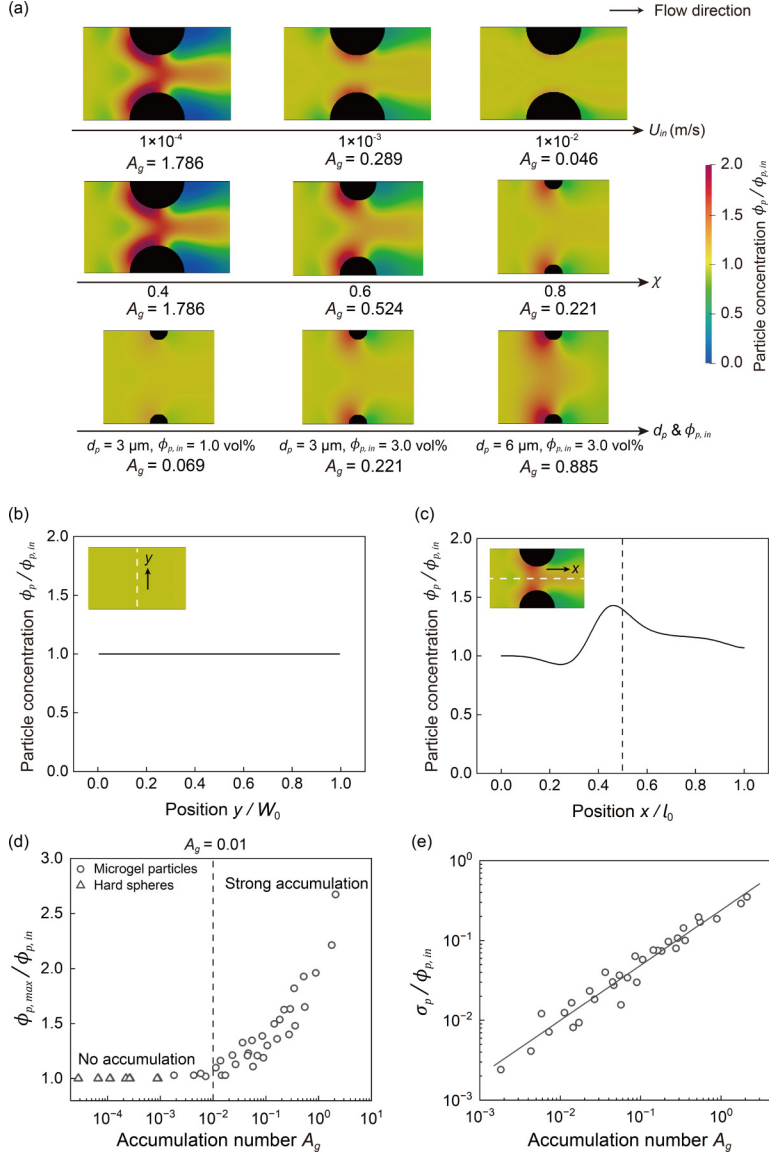


FIG. 2. Geometry-mediated accumulation in pore-throat geometries. (a) Examples showing the impacts of flow, structure, and particle property parameters on the accumulation state. The images are obtained from simulation results of microgel particle suspensions, and the values of A_g are calculated using Eq. (7a). The parameters for the example cases are as follows unless specified in the figure: $U_{in} = 10^{-4}$ m/s, $d_p = 3 \mu\text{m}$, $\phi_{p,in} = 3.0 \text{ vol}\%$, $\chi = 0.4$ for varying velocities and $\chi = 0.8$ for varying particle properties. (b), (c) Simulation results of microgel particle concentration distribution in (b) a straight channel and (c) a pore-throat geometry under the same condition, where W_0 is the channel width and l_0 is the channel length ($x/l_0 = 0.5$ corresponds to the throat center). The white dashed lines in the inset images denote the corresponding positions for statistics. Case information: $U_{in} = 10^{-4}$ m/s, $d_p = 3 \mu\text{m}$, $\phi_{p,in} = 1.0 \text{ vol}\%$, $\chi = 0.4$. (d) Variations in normalized maximum particle concentration $\phi_{p,max}/\phi_{p,in}$ vs the accumulation number A_g . The hard-sphere and microgel particle suspensions are denoted by the triangles and circles, respectively. A total of 72 numerical tests are conducted under various conditions. (e) Relationship between the accumulation intensity (characterized by the normalized standard deviation $\sigma_p/\phi_{p,in}$) and A_g .

The quantitative agreement between our numerical tests in typical particle systems and the theoretical model without fitting parameters evidence the generality of the geometry-mediated accumulation mechanism. As long as the suspension viscosity exhibits high sensitivity to particle concentration so that A_g is sufficiently high (> 0.01 based on numerous cases tested in this study), geometry-mediated accumulation should be pronounced regardless of the specific particle type. Beyond microgel particles in dilute conditions as an example, potential accumulation is also expected in red blood cell transport [30] and high-concentration flow of hard-sphere suspensions in porous media (see the Supplemental Material [29] for preliminary discussions).

B. Accumulation patterns and flow control mechanisms in heterogeneous porous media

We further investigate the transport of microgel particles governed by the geometry-mediated accumulation effect in a dual-permeability porous medium with representative preferential flow features. As shown in Fig. 3(a), the high-permeability layer (HPL) and low-permeability layer (LPL) yield the same porosity (45%) with a characteristic size ratio of 2:1. The minimum throat size is ten times larger than the maximum particle size. The inlet velocity is fixed considering computational cost, and the particle sizes and injection concentrations are varied as follows: $d_p = 3\text{--}6\text{ }\mu\text{m}$, $\phi_{p,\text{in}} = 1.0\text{--}5.0\text{ vol \%}$. The characteristic Stokes number is $\text{Stk} = \rho_p U_{\text{in}} d_p^2 / (18\mu_f W_{\text{in}}) = (2 \times 10^{-5})\text{--}(8 \times 10^{-5})$, where W_{in} is the inlet channel width.

For a heterogeneous structure, regions with lower permeability are more favorable for geometry-mediated accumulation of microgel particles. Since $U \propto K \propto W_{\text{pore}}^2$ for paralleled layers, where K is the intrinsic permeability, we have $\dot{\gamma} \sim U/W_{\text{pore}} \propto W_{\text{pore}}$. Therefore, the smaller characteristic width in the LPL and the higher characteristic viscosity induced by the lower shear rate will both contribute to a higher A_g , which leads to preferential accumulation, increases the local flow resistance, and intuitively exacerbates preferential flow.

Figure 3(b) summarizes concentration distribution patterns under various injection conditions. Distinct transitions between regimes are observed as particle size and injection concentration increase, corresponding to strengthened accumulation. To determine the transition criteria, we introduce the local geometric-mediated accumulation numbers $A_{g,h}$ and $A_{g,l}$ for different layers. The characteristic pore velocities in the HPL and LPL can be estimated as $U_h = U_{\text{in}} W_{\text{in}} / [W_{\text{sum},h} + (K_l/K_h)W_{\text{sum},l}]$, $U_l = (K_l/K_h)U_h$, where the subscripts l and h indicate the LPL and HPL, respectively, and W_{sum} is the total cross-sectional area of the pore space. As indicated in Fig. 3(b), the accumulation patterns align well with variations in $A_{g,h}$ and $A_{g,l}$, as the absolute value increases as injection concentration and particle size increase, while the relative magnitude $A_{g,l} > A_{g,h}$ is maintained. In Regime I, no significant accumulation is detected [Fig. 3(c)]. In Regime II, accumulation predominantly occurs throughout the LPL and at the edge region with lower characteristic speed. A relatively uniform global accumulation can be observed in the LPL, corresponding to in-depth penetration [Fig. 3(d)]. In Regime III, accumulation occurs in both layers but manifests differently. Weaker accumulation in the HPL is similar to the state of LPL in Regime II. Stronger accumulation in the LPL results in intensified local accumulation and limited penetration into the downstream region, showing a sharp increase followed by a rapid decrease in ϕ_p . Figure 3(e) presents quantitative statistics of the concentration distribution difference between global and localized accumulation. Note that the regime division here is not rigorous since particle accumulation patterns vary continuously in reality.

Intriguingly, the localized accumulation pattern resembles the formation of filter cakes reported in clogging events [9,45], even though clogging effects are excluded from our model. Here, these intense accumulation zones essentially reflect nonuniform concentration distributions, with particles remaining in motion driven by fluid drag, distinct from clogging and consistent with prior experimental observations [33]. As shown in the Supplemental Material [29], regions with localized intense accumulation can extend downstream as injection time increases, although at an extremely slow speed.

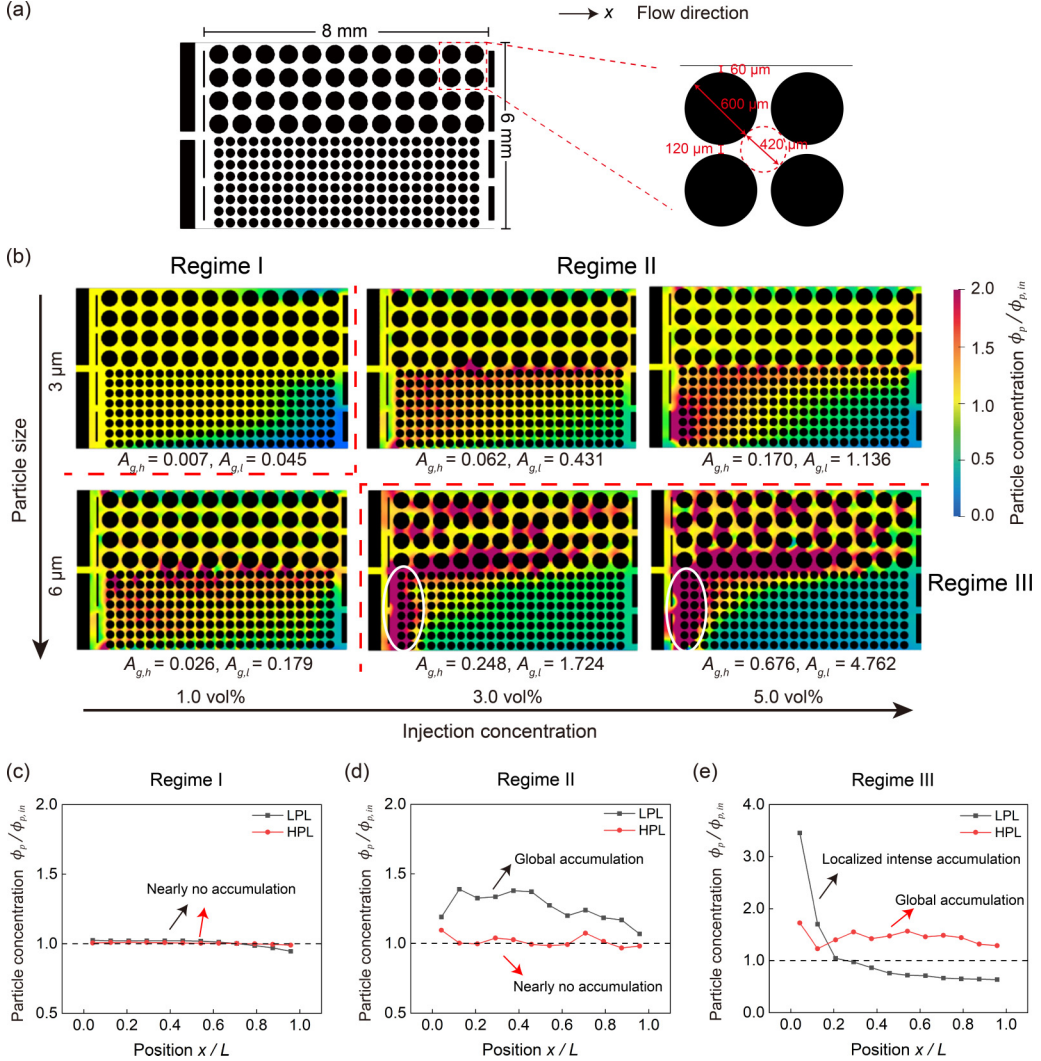


FIG. 3. (a) Case setup of the dual-permeability model with regular posts. The characteristic sizes in the low-permeability layer are half of those in the high-permeability layer. (b) Distribution patterns of micro-gel particle concentration after 1.8 PV (pore volume) of injection at various particle sizes and injection concentrations. The red dashed lines denote the transition between regimes, and the white circles denote regions with localized intense accumulation. (c)–(e) Typical concentration distributions in different layers in (c) Regime I ($d_p = 3 \mu\text{m}$, $\phi_p = 1.0 \text{ vol}\%$), (d) Regime II ($d_p = 6 \mu\text{m}$, $\phi_p = 1.0 \text{ vol}\%$), and (e) Regime III ($d_p = 6 \mu\text{m}$, $\phi_p = 3.0 \text{ vol}\%$). The black dashed lines denote the injection concentration.

Owing to the continuous pore size variations with history effects, building a quantitative correspondence between accumulation intensity and A_g is more difficult in comparison to the simplified pore-throat structures in Fig. 2. Nevertheless, the pattern transitions can be effectively captured by the dimensionless descriptions, with $A_{g,i} > 0.1$ and $A_{g,i} > 1$ approximately serving as the criteria for the onset of global accumulation and localized intense accumulation in layer i , respectively. We have also verified the generality of accumulation state transitions in the disordered medium, with clear dependences on particle size and concentration (see the Supplemental Material [29]). However, as the local throat-to-pore ratio varies significantly in disordered media, more quantitative

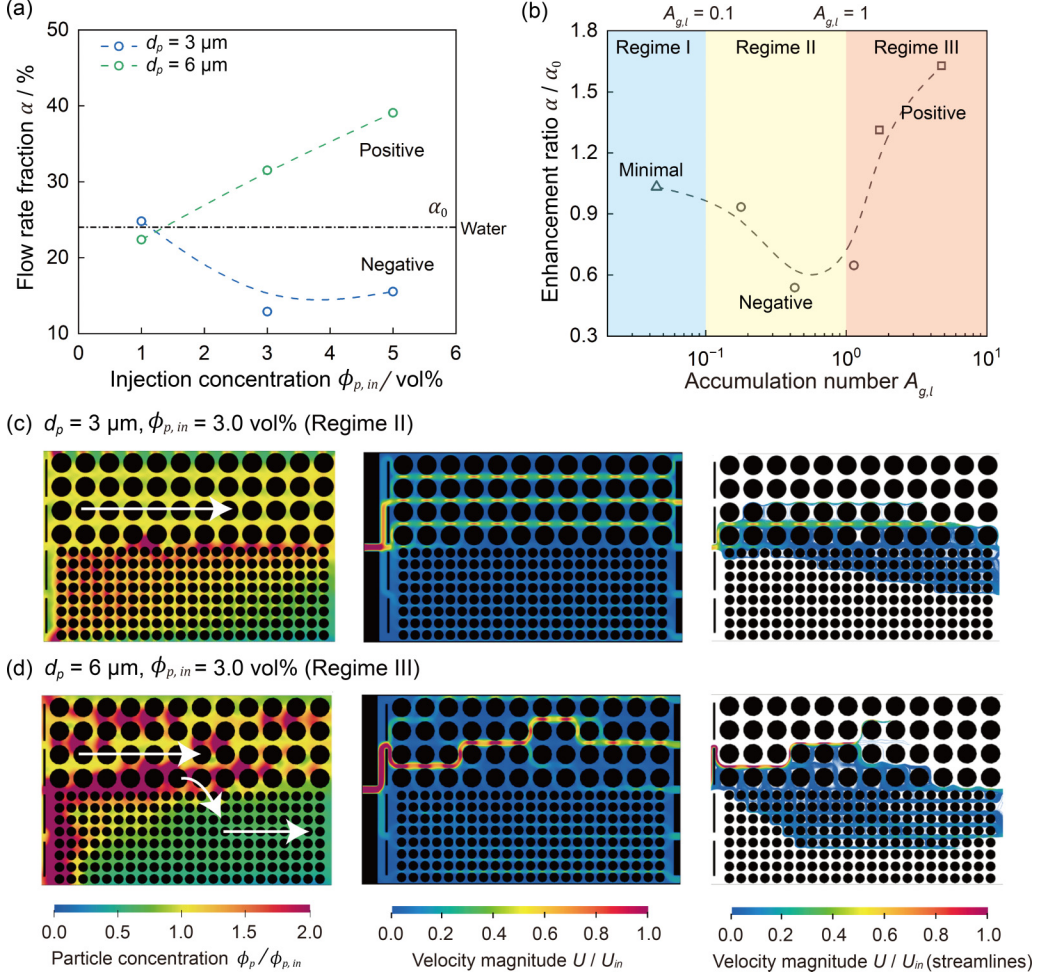


FIG. 4. Preferential flow control performances and mechanisms. (a) Evolution of the average flow rate fraction in the LPL vs injection concentration at different particle sizes. (b) Evolution of the enhancement ratio of the flow rate fraction in the LPL vs the geometry-mediated accumulation number of the LPL ($A_{g,l}$), corresponding to the regime transitions shown in Fig. 3. Preferential flow suppression (positive effect) corresponds to $\alpha/\alpha_0 > 1$. (c), (d) Comparison of particle concentrations, velocity fields, and streamlines passing through the interface between layers at representative cases. The white arrows in (d) illustrate lateral flow rate reallocation induced by the localized intense accumulation in the LPL.

predictions of the accumulation behaviors should be addressed in the future by improved upscaling tools inspired by the mechanisms interpreted in this work.

Quantification of preferential flow by the average flow rate fraction α in the LPL reveals a distinct size effect with water injection as a reference [Fig. 4(a)]. When $d_p = 3 \mu\text{m}$, preferential flow is exacerbated at high concentrations ($\phi_{p,in} \geq 3.0 \text{ vol}\%$), since less fluid is allocated into the LPL compared to water injection (α_0). Instead, the flow rate fraction in the LPL reaches a much higher level when $d_p = 6 \mu\text{m}$ under the same condition, indicating effective preferential flow control contrary to intuitive expectations.

As presented in Fig. 4(b), the intriguing transition from a negative to a positive effect on preferential flow is determined by the accumulation state evolution, which can be well characterized by the proposed accumulation number. In Regime II ($A_{g,h} < 0.1$, $0.1 < A_{g,l} < 1$), in-depth penetration

confined to the LPL corresponds to increased flow resistance in the LPL and strengthened preferential flow in the HPL [Fig. 4(c)]. In Regime III ($0.1 < A_{g,h} < 1$, $A_{g,l} > 1$), different accumulation states contribute to significant lateral flow between layers [Fig. 4(d)]. In the LPL, a localized high-concentration region forms near the inlet, whereas downstream concentration becomes extremely low. In the HPL, weaker accumulation effect results in the penetration and wide distribution of high-concentration regions. Although flow rate allocation at the inlet is hardly improved (see the velocity field distribution), the differences in accumulation states lead to a shift in flow resistance distribution and the formation of a new pathway inhibiting preferential flow. As illustrated by arrows in Fig. 4(d), fluid entering the HPL prefers to travel through the low-concentration region downstream in the LPL. More vertical streamlines covering a larger area in Fig. 4(d) compared to 4(c) confirm the presence of lateral flow. The nontrivial evolution of accumulation patterns and the resulting diversion effects dominated by particle behaviors significantly deviates from the feature of pure non-Newtonian solutions [46–48], where advection-diffusion should ultimately lead to a more uniform concentration field without pronounced pattern transitions.

C. Implications

As guidance for utilizing the mechanism interpretations regarding geometry-mediated accumulation effects, we summarize the key findings from our theoretical analysis and numerical simulations in various configurations as follows:

(1) Quantification of the dimensionless number: For any particle system with known rheological property, the accumulation number A_g can be directly quantified under given geometric (characteristic channel size and throat-to-pore ratio), flow (characteristic velocity), and suspension (particle size and concentration) conditions.

(2) Pore-scale triggering condition: For single pore-throat geometries, $A_g > 0.01$ can be approximately applied as the criterion for the triggering condition. The intensity of accumulation increases as A_g increases, which can be quantified by the nonuniformity of concentration distribution. Dramatic accumulation typically occurs for particle systems with pronounced viscosity effects such as microgel particle suspensions.

(3) Pattern transitions in porous media: In porous media, pattern transitions from insignificant accumulation, to global accumulation with in-depth penetration, and eventually to localized intense accumulation resembling filter cakes will occur as A_g increases. For the cases presented in this work, $A_g > 0.1$ and $A_g > 1$ approximately serve as the criteria for the onset of global accumulation and localized intense accumulation. Although the exact thresholds in disordered media may vary owing to continuous and complex pore size variations with history effects, the pattern transition behaviors should be consistent.

Flow diversion in heterogeneous porous media: In heterogeneous structures, different accumulation states in regions with different characteristic permeabilities lead to variations in flow diversion effects. As demonstrated in regular dual-permeability structures, only when the accumulation state falls in Regime III (global accumulation in the high-permeability region and localized intense accumulation in the low-permeability region), lateral flow significantly contributes to a new pathway inhibiting preferential flow.

VI. CONCLUSIONS

In summary, we investigate and highlight the unique role of geometry-mediated accumulation effects in dilute conditions, triggered by particle lagging in porous media under concentration-sensitive viscosity. Building on theoretical analysis and numerical simulations in typical pore-throat geometries and dual-permeability porous media, we comprehensively reveal the mechanisms underlying accumulation behaviors and flow consequences in porous media. Microscopically, the competition between the drag force representing fluid-particle interactions and the resistance force representing interparticle interactions determines the accumulation state. The proposed

dimensionless accumulation number quantifies the impacts of various influencing factors including flow, structure, and particle property parameters. Macroscopically, variable particle accumulation patterns in response to local geometric characteristics can self-adaptively adjust the resistance distribution in heterogeneous porous media. Lateral flow controlled by the distribution of localized intense accumulation zones is responsible for the preferential flow control performance. It is worth mentioning that particle accumulation induced by geometry variations has also been noticed in a recent work focusing on dense suspensions [49], where they investigate the transition to a high-particle-fraction “clogged” state based on a continuum approach.

Our study not only delves into the microscopic particle dynamics and macroscopic flow patterns regarding particle accumulation effects, but also paves the way for the effective modeling of complex fluid flow in porous media. Further efforts are required to unravel the combined effect of geometry-mediated accumulation, clogging, and particle deformation under more complex conditions such as multiphase displacement process. Regardless, we offer valuable insights into predicting and controlling particle transport in microchannels and porous media, with implications for membrane fouling prevention, hydrocarbon recovery enhancement, and microbial remediation of contaminated soil.

ACKNOWLEDGMENT

This work is financially supported by the NSF grants of China (Grants No. 12432013 and No. U24B6003).

DATA AVAILABILITY

The data that support the findings of this article are openly available [50].

-
- [1] T. Pak, L. F. d. L. Luz, T. Tosco, G. S. R. Costa, P. R. R. Rosa, and N. L. Archilha, Pore-scale investigation of the use of reactive nanoparticles for *in situ* remediation of contaminated groundwater source, [Proc. Natl. Acad. Sci. USA](#) **117**, 13366 (2020).
 - [2] J. Y. Parlange, Water transport in soils, [Annu. Rev. Fluid Mech.](#) **12**, 77 (1980).
 - [3] M. Elimelech and C. R. O’Melia, Kinetics of deposition of colloidal particles in porous media, [Environ. Sci. Technol.](#) **24**, 1528 (1990).
 - [4] R. C. Y. Koh and N. H. Brooks, Fluid mechanics of waste-water disposal in the ocean, [Annu. Rev. Fluid Mech.](#) **7**, 187 (1975).
 - [5] X. Lu and M. Wang, Shape and surface property effects on displacement enhancement by nanoparticles, [Int. J. Mech. Sci.](#) **255**, 108471 (2023).
 - [6] J. Schneider, R. D. Priestley, and S. S. Datta, Using colloidal deposition to mobilize immiscible fluids from porous media, [Phys. Rev. Fluids](#) **6**, 014001 (2021).
 - [7] I. L. Molnar, W. P. Johnson, J. I. Gerhard, C. S. Willson, and D. M. O’Carroll, Predicting colloid transport through saturated porous media: A critical review, [Water Resour. Res.](#) **51**, 6804 (2015).
 - [8] A. Farutin *et al.*, Optimal cell transport in straight channels and networks, [Phys. Rev. Fluids](#) **3**, 103603 (2018).
 - [9] E. Dressaire and A. Sauret, Clogging of microfluidic systems, [Soft Matter](#) **13**, 37 (2017).
 - [10] G. Gerber, S. Rodts, P. Aimeidieu, P. Faure, and P. Coussot, Particle-size-exclusion clogging regimes in porous media, [Phys. Rev. Lett.](#) **120**, 148001 (2018).
 - [11] V. Ramachandran and H. S. Fogler, Plugging by hydrodynamic bridging during flow of stable colloidal particles within cylindrical pores, [J. Fluid Mech.](#) **385**, 129 (1999).
 - [12] N. Bizmark, J. Schneider, R. D. Priestley, and S. S. Datta, Multiscale dynamics of colloidal deposition and erosion in porous media, [Sci. Adv.](#) **6**, eabc2530 (2020).

- [13] B. Bai, Y. Liu, J.-P. Coste, and L. Li, Preformed particle gel for conformance control: Transport mechanism through porous media, *SPE Reservoir Eval. Eng.* **10**, 176 (2007).
- [14] Q. Li and V. Prigiobbe, Numerical simulations of the migration of fine particles through porous media, *Transp. Porous Media* **122**, 745 (2018).
- [15] J. Leng, M. Wei, and B. Bai, Review of transport mechanisms and numerical simulation studies of preformed particle gel for conformance control, *J. Pet. Sci. Eng.* **206**, 109051 (2021).
- [16] C. Henry, J.-P. Minier, and G. Lefèvre, Towards a description of particulate fouling: From single particle deposition to clogging, *Adv. Colloid Interface Sci.* **185-186**, 34 (2012).
- [17] C. E. Brennen, *Fundamentals of Multiphase Flow* (Cambridge University Press, Cambridge, 2005).
- [18] D. L. Koch and R. J. Hill, Inertial effects in suspension and porous-media flows, *Annu. Rev. Fluid Mech.* **33**, 619 (2001).
- [19] L.-P. Wang, A. S. Wexler, and Y. Zhou, Statistical mechanical description and modelling of turbulent collision of inertial particles, *J. Fluid Mech.* **415**, 117 (2000).
- [20] D. Gidaspow, *Multiphase Flow and Fluidization: Continuum and Kinetic Theory Descriptions* (Academic, New York, 1994).
- [21] L. Xie and Z.-H. Luo, Modeling and simulation of the influences of particle-particle interactions on dense solid-liquid suspensions in stirred vessels, *Chem. Eng. Sci.* **176**, 439 (2018).
- [22] A. Karnis, H. L. Goldsmith, and S. G. Mason, The kinetics of flowing dispersions: I. Concentrated suspensions of rigid particles, *J. Colloid Interface Sci.* **22**, 531 (1966).
- [23] C. J. Koh, P. Hookham, and L. G. Leal, An experimental investigation of concentrated suspension flows in a rectangular channel, *J. Fluid Mech.* **266**, 1 (1994).
- [24] P. R. Nott and J. F. Brady, Pressure-driven flow of suspensions: Simulation and theory, *J. Fluid Mech.* **275**, 157 (1994).
- [25] D. Lhuillier, Migration of rigid particles in non-brownian viscous suspensions, *Phys. Fluids* **21**, 023302 (2009).
- [26] P. R. Nott, E. Guazzelli, and O. Pouliquen, The suspension balance model revisited, *Phys. Fluids* **23**, 043304 (2011).
- [27] É. Guazzelli and O. Pouliquen, Rheology of dense granular suspensions, *J. Fluid Mech.* **852**, P1 (2018).
- [28] I. M. Krieger and T. J. Dougherty, A mechanism for non-Newtonian flow in suspensions of rigid spheres, *J. Rheol.* **3**, 137 (1959).
- [29] See Supplemental Material at <http://link.aps.org/supplemental/10.1103/834p-q9hf> for discussions on model parameters, details of numerical method, simulation and case setup, and discussions on simulation results, which includes Refs. [27,28,32,33,51–70].
- [30] D. E. Brooks, J. W. Goodwin, and G. V. Seaman, Interactions among erythrocytes under shear, *J. Appl. Physiol.* **28**, 172 (1970).
- [31] H. Wang, M. Lin, D. Chen, Z. Dong, Z. Yang, and J. Zhang, Research on the rheological properties of cross-linked polymer microspheres with different microstructures, *Powder Technol.* **331**, 310 (2018).
- [32] Q. Li, G. Yang, Y. Huang, X. Lu, J. Min, and M. Wang, Lattice Boltzmann method for particulate multiphase flow system, *Int. J. Mech. Sci.* **273**, 109217 (2024).
- [33] W. Lei, Q. Li, H.-E. Yang, T.-J. Wu, J. Wei, and M. Wang, Preferential flow control in heterogeneous porous media by concentration-manipulated rheology of microgel particle suspension, *J. Pet. Sci. Eng.* **212**, 110275 (2022).
- [34] K. Spildo, A. Skauge, M. G. Aarra, and M. T. Tweheyo, A new polymer application for north sea reservoirs, *SPE Reservoir Eval. Eng.* **12**, 427 (2009).
- [35] M. A. E. Kokubun, F. A. Radu, E. Keilegavlen, K. Kumar, and K. Spildo, Transport of polymer particles in oil–water flow in porous media: Enhancing oil recovery, *Transp. Porous Media* **126**, 501 (2019).
- [36] D. A. Drew, Mathematical modeling of two-phase flow, *Annu. Rev. Fluid Mech.* **15**, 261 (1983).
- [37] M. A. van der Hoef, M. van Sint Annaland, N. G. Deen, and J. A. M. Kuipers, Numerical simulation of dense gas-solid fluidized beds: A multiscale modeling strategy, *Annu. Rev. Fluid Mech.* **40**, 47 (2008).
- [38] R. Jackson, Locally averaged equations of motion for a mixture of identical spherical particles and a Newtonian fluid, *Chem. Eng. Sci.* **52**, 2457 (1997).

- [39] J. Ding and D. Gidaspow, A bubbling fluidization model using kinetic theory of granular flow, *AIChE J.* **36**, 523 (1990).
- [40] W. Shuai, H. Zhenhua, L. Huilin, L. Goudong, W. Jiaying, and X. Pengfei, A bubbling fluidization model using kinetic theory of rough spheres, *AIChE J.* **58**, 440 (2012).
- [41] C. Y. Wen and Y. H. Yu, *Chemical Engineering Progress Symposium Series* (American Institute of Chemical Engineers, New York, 1966), p. 100.
- [42] H. Grad, On the kinetic theory of rarefied gases, *Commun. Pure Appl. Math.* **2**, 331 (1949).
- [43] C. K. K. Lun, S. B. Savage, D. J. Jeffrey, and N. Chepur, Kinetic theories for granular flow: Inelastic particles in Couette flow and slightly inelastic particles in a general flowfield, *J. Fluid Mech.* **140**, 223 (1984).
- [44] Z. Adamczyk and P. Weroński, Application of the DLVO theory for particle deposition problems, *Adv. Colloid Interface Sci.* **83**, 137 (1999).
- [45] A. Sauret, K. Somszor, E. Villermaux, and E. Dressaire, Growth of clogs in parallel microchannels, *Phys. Rev. Fluids* **3**, 104301 (2018).
- [46] W. M. Jones, Polymer additives in reservoir flooding for oil recovery: Shear thinning or shear thickening? *J. Phys. D: Appl. Phys.* **13**, L87 (1980).
- [47] R. B. Needham and P. H. Doe, Polymer flooding review, *J. Pet. Technol.* **39**, 1503 (1987).
- [48] C. Xie, W. Lei, M. T. Balhoff, M. Wang, and S. Chen, Self-adaptive preferential flow control using displacing fluid with dispersed polymers in heterogeneous porous media, *J. Fluid Mech.* **906**, A10 (2021).
- [49] A. A. Herale, P. Pearce, and D. R. Hewitt, Emergent clogging of continuum particle suspensions in constricted channels, *J. Fluid Mech.* **1017**, A24 (2025).
- [50] X. Lu, Q. Li, G. Yang, Y. Huang, W. Lei, and M. Wang, Mendeley data (2025), doi:10.17632/kms4f9gbpr.1.
- [51] G. K. Batchelor and J. T. Green, The hydrodynamic interaction of two small freely-moving spheres in a linear flow field, *J. Fluid Mech.* **56**, 375 (1972).
- [52] F. Ferrini, D. Ercolani, B. de Cindio, L. Nicodemo, L. Nicolais, and S. Ranaudo, Shear viscosity of settling suspensions, *Rheol. Acta* **18**, 289 (1979).
- [53] G. K. Batchelor, Sedimentation in a dilute dispersion of spheres, *J. Fluid Mech.* **52**, 245 (1972).
- [54] P. Lallemand and L.-S. Luo, Theory of the lattice Boltzmann method: Dispersion, dissipation, isotropy, galilean invariance, and stability, *Phys. Rev. E* **61**, 6546 (2000).
- [55] Z. Guo, C. Zheng, and B. Shi, Discrete lattice effects on the forcing term in the lattice Boltzmann method, *Phys. Rev. E* **65**, 046308 (2002).
- [56] V. Semiao and G. Silva, First- and second-order forcing expansions in a lattice Boltzmann method reproducing isothermal hydrodynamics in artificial compressibility form, *J. Fluid Mech.* **698**, 282 (2012).
- [57] Z. Yu and L.-S. Fan, Multirelaxation-time interaction-potential-based lattice Boltzmann model for two-phase flow, *Phys. Rev. E* **82**, 046708 (2010).
- [58] T. Wang and J. Wang, Two-fluid model based on the lattice Boltzmann equation, *Phys. Rev. E* **71**, 045301(R) (2005).
- [59] S. Leclaire, M. Reggio, and J.-Y. Trépanier, Isotropic color gradient for simulating very high-density ratios with a two-phase flow lattice Boltzmann model, *Comput. Fluids* **48**, 98 (2011).
- [60] C. Xie, J. Zhang, V. Bertola, and M. Wang, Lattice Boltzmann modeling for multiphase viscoplastic fluid flow, *J. Non-Newtonian Fluid Mech.* **234**, 118 (2016).
- [61] X. Lu and M. Wang, High-performance nanogel-in-oils as emulsion evolution controller for displacement enhancement in porous media, *ACS Appl. Mater. Interfaces* **15**, 49554 (2023).
- [62] B. K. Aral and D. M. Kalyon, Effects of temperature and surface roughness on time-dependent development of wall slip in steady torsional flow of concentrated suspensions, *J. Rheol.* **38**, 957 (1994).
- [63] P. Ballesta, G. Petekidis, L. Isa, W. C. K. Poon, and R. Besseling, Wall slip and flow of concentrated hard-sphere colloidal suspensions, *J. Rheol.* **56**, 1005 (2012).
- [64] F. Soltani and Ü. Yilmazer, Slip velocity and slip layer thickness in flow of concentrated suspensions, *J. Appl. Polym. Sci.* **70**, 515 (1998).

- [65] F. Qin, L. Fei, J. Zhao, Q. Kang, D. Derome, and J. Carmeliet, Lattice Boltzmann modelling of colloidal suspensions drying in porous media accounting for local nanoparticle effects, [J. Fluid Mech. **963**, A26 \(2023\)](#).
- [66] M. Residori, S. Praetorius, P. de Anna, and A. Voigt, Influence of finite-size particles on fluid velocity and transport through porous media, [Phys. Rev. Fluids **8**, 074501 \(2023\)](#).
- [67] J. Su, Z. Gu, and X. Y. Xu, Discrete element simulation of particle flow in arbitrarily complex geometries, [Chem. Eng. Sci. **66**, 6069 \(2011\)](#).
- [68] Q. Zou and X. He, On pressure and velocity boundary conditions for the lattice Boltzmann BGK model, [Phys. Fluids **9**, 1591 \(1997\)](#).
- [69] Q. Lou, Z. Guo, and B. Shi, Evaluation of outflow boundary conditions for two-phase lattice Boltzmann equation, [Phys. Rev. E **87**, 063301 \(2013\)](#).
- [70] M. Wang, J. Wang, N. Pan, and S. Chen, Mesoscopic predictions of the effective thermal conductivity for microscale random porous media, [Phys. Rev. E **75**, 036702 \(2007\)](#).